Journal of Computational Physics 295 (2015) 805–814

Contents lists available at ScienceDirect

Journal of Computational Physics

www.elsevier.com/locate/jcp

Numerically accurate computation of the conditional trajectories of the topological invariants in turbulent flows

Adrián Lozano-Durán [a,*], Markus Holzner [b], Javier Jiménez [a]

[a] School of Aeronautics, U. Politécnica de Madrid, 28040 Madrid, Spain
[b] ETH Zurich, 8093 Zurich, Switzerland

ARTICLE INFO

Article history:
Received 12 February 2015
Accepted 25 April 2015
Available online 30 April 2015

Keywords:
Turbulence
Velocity gradient tensor
Invariants
CMTs

ABSTRACT

The computation of the topological invariants of the velocity gradient tensor and of their conditional mean trajectories in incompressible turbulent flows is revisited. It is argued that probability conservation requires that the conditional mean trajectories should be closed when a statistically stationary wall-bounded or periodic domain is considered, and this is confirmed numerically for a turbulent channel. It is argued that previous reports of inward spiraling of the conditional trajectories are either due to incomplete statistics in inhomogeneous flows or to numerical errors.

1. Introduction

Many fundamental properties of turbulent flows are encoded in the gradients of the velocity, which provide important information regarding the local behavior of the flow. The invariants of the velocity gradient tensor for incompressible flows, R and Q, were first introduced in [1] and have proven to be a useful tool to analyze turbulent flows characterized by a wide spectrum of scales, e.g. [1–9]. They quantify the relative strength of enstrophy production and strain self-amplification, and of local enstrophy density and strain density respectively. Moving locally with a fluid particle, the velocity gradient tensor determines the linear approximation to the local velocity field surrounding the observer. In that frame, invariants can also be used to classify the local flow topology, as shown in [1].

R and Q are challenging quantities to obtain from both the numerical and experimental point of view, since they involve products of the velocity gradients and it is crucial to represent accurately the high wavenumbers. Nevertheless, they have been measured experimentally and computed numerically numerous times. Results from different turbulent flows showed that the joint probability density function of R and Q has a very particular skewed 'tear drop' shape, e.g. [10,11,2,3]. That is, there is an increased probability of points where $R > 0$ and $Q < 0$ along the so-called Vieillefosse tail. Such a signature turns out to be a quite universal feature persistent in many different turbulent flows, including mixing layers [10], channel flows [12], boundary layers [13,7], homogeneous isotropic turbulence [14,11], etc.

References [14] and [11] introduced and studied the conditional mean trajectories of the invariants (henceforth, CMTs) in direct numerical simulations of homogeneous isotropic turbulence at low Reynolds numbers. This involved the calculation of the mean temporal rate of change of the invariants conditioned on the values of the invariants themselves, and gives a vector field in the R–Q plane. The resulting conditional vector field can be integrated to produce trajectories within the

* Corresponding author.
E-mail address: adrian@torroja.dmt.upm.es (A. Lozano-Durán).

http://dx.doi.org/10.1016/j.jcp.2015.04.036

space of the pair of the invariants. The computation of this vector field is even more challenging than the one of R and Q since it requires calculating their material derivative.

The analysis of the CMTs yields information about the dynamics of the small scales of turbulence. Previous results suggested a cyclic and approximately periodic orbit with a mean clockwise evolution in the R–Q plane and trajectories spiraling towards $(R, Q) = (0, 0)$. Some authors have conjectured about the spurious nature of the spiraling of the CMTs towards the origin [14]. However, others have argued that this effect may have a physical significance related to the statistical tendency of the flow to form shear layers [15] and the question remains open. The time-scale associated with the CMTs is also considered representative of the cycle involved in the dynamics of turbulence and has been computed in [14,11,6,15] and [7] among others.

The dynamical evolution of the velocity gradient tensor, and hence, the accurate computation of the CMTs, is also fundamental for the development of statistical models (see [16] and references therein). Due to its simplicity, one of the first models was the Restricted Euler Model [17,18], where the influence of the pressure and viscosity is neglected. Its solution was later obtained and analyzed in [19] but it showed neither closed nor spiraling CMTs and its oversimplified dynamics resulted in a qualitatively different picture from that obtained in simulated and experimental results. Later attempts focused on more sophisticated models which reproduced more realistic CMTs without determining whether the trajectories should or should not be closed [16]. It is clear that these models should be conceptually different depending on the nature of the CMTs, and from there derives the importance of its study.

In this paper, we study the numerical requirements for the accurate computation of the invariants of the velocity gradient tensor in turbulent channel flows and its implications in the CMTs. The effects of the normalization of the invariants and of the inhomogeneity of the flow are addressed too. It is also analyzed which are the necessary conditions for the CMTs to form closed trajectories.

The paper is organized as follows. The invariants of the velocity gradient tensor and the conditions to form closed CMTs are discussed in Section 2. The numerical experiments and methods are presented in Section 3. Results are offered in Section 4, which is divided in three subsections. Section 4.1 is devoted to the numerical analysis of the computation of the invariants and its material derivatives, Section 4.2 to the effect of the normalization, and Section 4.3 to the consequences of conditioning the statistics on sub-domains in inhomogeneous flows. Finally, we close with the conclusions in Section 5.

2. Invariants of the velocity gradient tensor and probability conservation

The invariants of the velocity gradient tensor for an incompressible flow, Q and R, are

$$Q = \frac{1}{4}(\omega_i\omega_i - 2s_{ij}s_{ij}), \tag{1}$$

$$R = -\frac{1}{3}s_{ij}s_{jk}s_{ki} - \frac{1}{4}\omega_i\omega_j s_{ij}, \tag{2}$$

where summation over repeated indices is implied, ω_i are the components of the vorticity vector and s_{ij} of the rate-of-strain tensor.

The invariants R and Q defined by relations (1) and (2) may be interpreted in two ways. From a physical point of view, Q measures the relative importance of enstrophy and strain densities. Enstrophy dominates over strain for positive and large values of Q, and strain does for negative and large ones. The meaning of R depends on the value of Q. For $Q > 0$ and large, $R < 0$ represents vortex stretching and $R > 0$ vortex compression. For $Q < 0$ and large, R is dominated by the strain self-amplification. The second interpretation is topological, R and Q characterize the local motion of the fluid particles for an observer traveling with the fluid. The lines $D = 27/4R^2 + Q^3 = 0$ and $R = 0$ divide the R–Q plane in four regions (see Fig. 2(a)). The trajectories of the fluid particles are then classified according to critical point terminology [1], as stable focus/stretching (upper left-hand region), unstable focus/compressing (upper right-hand region), stable node/saddle/saddle (lower left-hand region) and unstable node/saddle/saddle (lower right-hand region).

The conditional mean trajectories or CMTs [14] aim to study the Lagrangian temporal evolution of the invariants. The method relies on calculating the averaged time rates of change of the invariants for the fluid particles, $\mathrm{D}R/\mathrm{D}t$ and $\mathrm{D}Q/\mathrm{D}t$, conditioned on the values of R and Q. Note that $\mathrm{D}/\mathrm{D}t$ stands for material derivative. These quantities can be thought of as the components of a conditionally averaged vector field in the R–Q plane,

$$\boldsymbol{v} = \left\langle \left(\frac{\mathrm{D}R}{\mathrm{D}t}, \frac{\mathrm{D}Q}{\mathrm{D}t} \right) \right\rangle_{R,Q}, \tag{3}$$

where $\langle\cdot\rangle_{R,Q}$ denotes conditional average at point (R, Q). From $\boldsymbol{v}$, any chosen initial condition can be integrated resulting in the aforementioned CMTs.

If we define $J(R, Q)$ as the joint probability density function of R and Q, the equation for the conservation of probability states that

$$\frac{\partial J}{\partial t} + \begin{pmatrix} \frac{\partial}{\partial R} \\ \frac{\partial}{\partial Q} \end{pmatrix} \cdot \boldsymbol{\mathcal{W}} = 0, \tag{4}$$

where $\mathcal{W} = J\boldsymbol{v}$ is the 'probability current'. Eq. (4) is satisfied when two conditions are met. First, R and Q must be smooth functions of time, which is guaranteed since they satisfy a differential equation. Second, the flux of probability crossing the boundaries of the domain must be zero. This is the case when the domain is delimited by walls or periodic boundaries, or when the flow is homogeneous and isotropic. Previous works [20] have used a Fokker–Planck equation [21] to characterize the dynamics of $J(R, Q)$, which reduces to Eq. (4) when applied to a deterministic system.

If the second condition is not fulfilled, for instance, when considering only the flow contained on a spatial sub-domain, Ω, Eq. (4) must be modified to include the change of probability caused by the effect of the boundaries

$$\frac{\partial J_\Omega}{\partial t} + \begin{pmatrix} \frac{\partial}{\partial R} \\ \frac{\partial}{\partial Q} \end{pmatrix} \cdot \mathcal{W}_\Omega = \phi_\Omega, \tag{5}$$

where J_Ω is the joint probability of R and Q in Ω, and $\phi_\Omega = \phi_\Omega(R, Q)$ a function representing sources and sinks that accounts for the R and Q crossing the boundaries of the sub-domain. For homogeneous isotropic turbulence, this term is zero regardless of the sub-domain, but the same is not true for certain regions in inhomogeneous flows, for example, the one comprised between two wall-parallel planes located at different heights in a turbulent channel.

For statistically stationary conditions, the temporal change of $J(R, Q)$ in Eq. (4) vanishes and the probability current must be divergence-free

$$\begin{pmatrix} \frac{\partial}{\partial R} \\ \frac{\partial}{\partial Q} \end{pmatrix} \cdot \mathcal{W} = 0. \tag{6}$$

This implies that the streamlines of the vector field $\mathcal{W}$ are closed. It is important to note that if the streamlines of $\mathcal{W}$ are closed so are those of $\boldsymbol{v}$ (and hence the CMTs) since $J(R, Q)$ is guaranteed to be a non-negative function that only changes the magnitude of the vector field $\boldsymbol{v}$ at each (R, Q) point but not its direction nor its orientation. As a result, the streamlines of $\boldsymbol{v}$ and $\mathcal{W}$ are identical. This occurs even if $\boldsymbol{v}$ is not divergence-free, and it shows that the CMTs are closed in domains delimited by walls or periodic boundaries, or in homogeneous and isotropic flows. We will use this property in the upcoming sections to test the errors of the computed CMTs.

The last remark is about the relationship between the iso-probability contours of $J(R, Q)$ and the CMTs in the stationary state. Expanding Eq. (6) yields

$$\boldsymbol{v} \cdot \begin{pmatrix} \frac{\partial J}{\partial R} \\ \frac{\partial J}{\partial Q} \end{pmatrix} = -J \begin{pmatrix} \frac{\partial}{\partial R} \\ \frac{\partial}{\partial Q} \end{pmatrix} \cdot \boldsymbol{v} \tag{7}$$

and proves that the iso-probability contours of $J(R, Q)$ and the CMTs are not parallel because the product of the gradient of $J(R, Q)$ by the vector field $\boldsymbol{v}$ is not zero in general.

3. Numerical experiments

We use data from a direct numerical simulation (DNS) of a turbulent channel flow from [22] at a friction Reynolds number $Re_\tau = u_\tau h/\nu = 932$, where u_τ is the friction velocity, h the channel half-height and ν the kinematic viscosity. The superscript $+$ denotes wall units based on u_τ and ν. The parameters of the simulation are summarized in Table 1 where x, y and z are the streamwise, wall-normal and spanwise directions respectively, with associated velocities u, v and w. The incompressible flow is integrated in the form of evolution equations for the wall-normal vorticity and for the Laplacian of the wall-normal velocity [23] and the spatial discretization is Fourier in the two wall-parallel directions using the 3/2 dealiasing rule. Chebyshev polynomials are used in the y direction. Time stepping is performed with a third-order semi-implicit Runge–Kutta scheme [24]. The DNS was run for 20 eddy turnover times, h/u_τ, and the fields were stored with a temporal spacing of $0.05h/u_\tau$ between consecutive snapshots.

We used different numerical approaches to compute the invariants of the velocity gradient and their material derivatives from the DNS presented above. All the calculations are performed in double precision and multiple spatial resolutions and temporal numerical schemes are used to assess the effect of the numerical accuracy.

The spatial derivatives are computed using spectral methods: Fourier in x and z and Chebyshev in y. Since the computation of the invariants involves double and triple products of the velocity gradients, we will test the effect of different spatial resolutions. Therefore, the number of modes of the velocity field from the DNS in Table 1 is increased and padded with zeros before computing the invariants. Three cases are considered, expanding the number of modes by a factor of 3/2 only in x and z, or by a factor of 2 or 3 in all the directions. We will refer to these cases as 3/2-, 2- and 3-expansion. The first case is the usual scenario in those DNSs using the 3/2-rule for dealiasing. Note that expanding the number of modes in each direction by a factor of 3 increases the computational cost by a factor of 27 in both memory and CPU usage.

The material derivatives of R and Q are computed in the form

$$\mathrm{D}/\mathrm{D}t = \partial/\partial t + \boldsymbol{u} \cdot \nabla, \tag{8}$$

where $\boldsymbol{u}$ is the velocity flow field and ∇ the gradient operator numerically computed as described above. For the time derivative, several extra fields were generated for each flow field advancing the DNS in time with a constant time step, Δt.

Table 1
Parameters of the simulation: L_x and L_z are the streamwise and spanwise dimensions of the numerical box and h is the channel half-height; Δx and Δz are the resolutions in terms of Fourier modes before dealiasing; N_x, N_y and N_z are the number of streamwise, wall-normal and spanwise modes respectively; N_f is the number of flow fields separated by $0.05h/u_\tau$ used to accumulate statistics and Tu_τ/h the total time simulated in eddy turnovers.

Re_τ	L_x/h	L_z/h	Δx^+	Δz^+	N_x	N_y	N_z	N_f	Tu_τ/h
932	2π	π	11	5.7	512	385	512	400	20

Table 2
Parameters of the cases used to compute the invariants and study their numerical errors. N_x, N_y and N_z are the number of streamwise, wall-normal and spanwise modes respectively; In fifth column, *Order* refers to the order of the finite differences scheme used to compute $\partial R/\partial t$ and $\partial Q/\partial t$. CFL is the average Courant–Friedrichs–Lewy number used to calculate the extra flow fields required for the time derivatives. Cases E1, E2 and E3 are intended to test the spatial accuracy and the rest the temporal one.

Case	N_x	N_y	N_z	*Order*	CFL
E1	768	385	768	4th	0.075
E2	1024	769	1024	4th	0.075
E3	1536	1153	1536	4th	0.075
F1L	1536	1153	1536	1st	0.750
F1S	1536	1153	1536	1st	0.075
F2L	1536	1153	1536	2nd	0.750
F2S	1536	1153	1536	2nd	0.075

The generated fields are then used to compute $\partial R/\partial t$ and $\partial Q/\partial t$ with finite differences. Three numerical schemes are tested: first-order forward, second-order centered and fourth-order centered finite differences, for which it was necessary to generate two, three and five extra flow fields respectively. Besides, two different time steps are analyzed, $\Delta t^+ = 4 \cdot 10^{-2}$ and $\Delta t^+ = 4 \cdot 10^{-3}$ that on average correspond to CFL = 0.75 and CFL = 0.075. Another approach to compute the material derivatives is through the right-hand side of the dynamical equations of the invariants used by many works, especially in those dealing with isotropic turbulence where the pressure can be easily obtained [14]. In the present work, we prefer to use directly the relation (8) and avoid the calculation of the pressure. The comparison of both methods could be an interesting question for future publications.

The different numerical scenarios for computing the invariants and their material derivatives are summarized in Table 2. The cases are divided in two blocks. Those in the first block are intended to test the effect of the spatial numerical accuracy and are denoted by Eγ, where γ is equal to 1, 2 or 3 corresponding to a 3/2-, 2- or 3-expansion respectively. The cases in the second block aim to test the temporal numerical accuracy and are named as F$\beta\omega$, where β takes the values of 1, 2 depending on whether the finite differences scheme used to compute the time derivative is 1st or 2nd order accurate, respectively, and ω is either L (long) for $\Delta t^+ = 4 \cdot 10^{-2}$ (CFL = 0.75) or S (short) for $\Delta t^+ = 4 \cdot 10^{-3}$ (CFL = 0.075). The results are presented and analyzed in the next section.

All the CMTs shown in this work are obtained by integrating the trajectory of a virtual particle in the R–Q plane with a time-marching Runge–Kutta–Feylberg scheme with a relative error of 10^{-6}, and interpolating the vector field $\boldsymbol{v}$ with cubic splines.

4. Results

4.1. Effect of the numerical accuracy

We discuss the impact of the numerics in R, Q and the CMTs. All the results presented in this section are computed for the whole channel. First, we focus on the spatial accuracy. This corresponds to the first three cases in Table 2, E1, E2 and E3, which are computed with high accuracy in time using a fourth-order finite differences scheme to minimize the errors from the time derivatives, but with different number of modes in space.

The numerically most challenging quantity is DR/Dt, which involves the material derivative of cubes of the velocity gradients. Figs. 1(a, b, c) show snapshots of DR/Dt at the same wall-parallel plane for the three cases. The aliasing errors are evident when the usual 3/2-expansion is applied and are alleviated with the 2-expansion. The anisotropy observed in the distribution of errors in the latter case (Fig. 1(b)) is probably caused by the coarser resolution in the x direction which is twice larger than the one in z (see Tables 1 and 2). The best results are attained for the 3-expansion, although DR/Dt could contain wavenumbers up to four times higher than those of the original velocity field. An extra case was computed (not shown) expanding the number of modes in each direction by a factor of 4, and very similar results were obtained compared to those for the 3-expansion.

In addition to the instantaneous snapshots of DR/Dt, we are interested in the statistical properties of R and Q. Fig. 1(d) shows the root-mean-squared fluctuating R and Q, $R'(y)$ and $Q'(y)$, as functions of the wall-normal distance. The results are indistinguishable for the three cases. We will use the wall-normal average of $Q'(y)$, denoted by $\overline{Q'}$, to normalized Q and R in the following plots. Fig. 2(a) contains the iso-probability contours of the joint probability density function (p.d.f.)

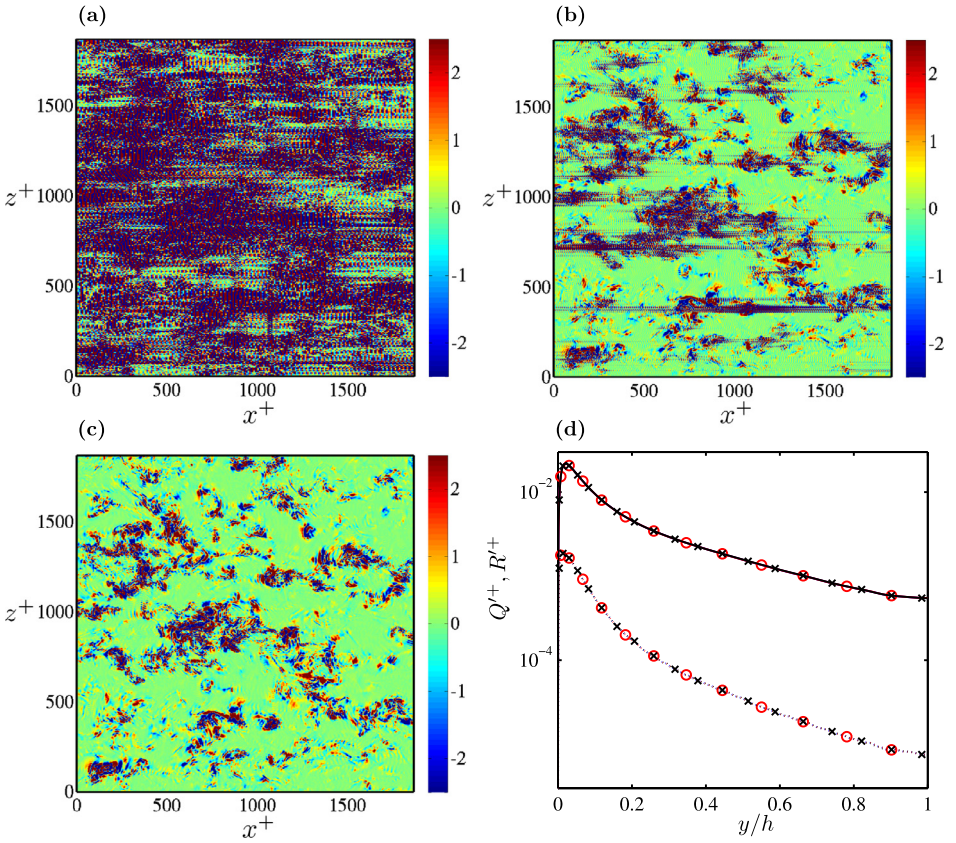

Fig. 1. Example of an instantaneous wall-parallel plane of DR/Dt at $y/h = 0.25$ for (a), 3/2-expansion; (b), 2-expansion and (c), 3-expansion. The colorbars are in wall units. (d) Root-mean-squared fluctuating Q (solid) and R (dashed) as a function of the wall-normal distance, y. Symbols and lines are ———, case E1 (3/2-expansion); ∘, case E2 (2-expansion) and ×, case E3 (3-expansion).

of R and Q, and again the differences are negligible between the three cases. From the previous results, we conclude that the one-point statistics of the invariants and their joint p.d.f.s are insensitive to expanding the number of modes.

Unfortunately, the vector field $\boldsymbol{v}$ and the CMTs are affected by the spatial resolution as shown in Figs. 2(b, c, d). This is especially the case when the modes are only expanded by a factor of 3/2 in the x and z directions (Fig. 2(b)) which is the common practice in numerical computations. As a consequence, the CMTs deform and do not close. This spurious behavior almost vanishes when the number of modes in each direction is expanded by the factor of 2 (Fig. 2(c)), and it completely disappears when the factor is 3 (Fig. 2(d)). The results from the latter case are consistent with the discussion in Section 2, where it was argued that the CMTs must close when the whole channel is considered and the numerical errors are negligible. As far as we know, this is the first time closed CMTs have been reported.

We assess next the effects of the numerical errors on the time derivatives $\partial R/\partial t$ and $\partial Q/\partial t$. In order to do so, let us consider the last four cases from Table 2, which are computed with high spatial resolution (3-expansion) to maintain the spatial numerical errors to a minimum. There are two degrees of freedom in the temporal analysis, that are the time step (or the averaged CFL) between the consecutive flow fields and the order of accuracy of the finite differences scheme. We will consider two time steps and two orders of accuracy, which are summarized in Table 2 as cases F1L, F1S, F2L and F2S.

The results are shown in Figs. 3(a, b, c, d). For CFL = 0.75 and the first-order accurate scheme, the velocity in $R-Q$ plane follows a clockwise evolution that is quite strongly convergent towards the origin (Fig. 3(a)). Fig. 3(b) shows that a reduction from CFL = 0.75 to CFL = 0.075 has indeed a significant effect on the CMTs, and the spiraling is cured to a moderate extent. Huge improvements are achieved by increasing the order of accuracy to second-order for both time steps. Comparing case E3 (fourth-order accurate and CFL = 0.075) from Fig. 2(d) with case F2S (second-order accurate and CFL = 0.075) from Fig. 3(d) shows that a further increase of the order of the scheme has a relatively weak effect.

The spiraling effect of the CMTs is quantified by comparing the initial distance of the orbits from the origin in the $Q-R$ plane, r_0, with the distance after one full revolution, $r_{2\pi}$, where $r = \sqrt{Q^2 + R^2}$. The ratio $r_{2\pi}/r_0$ is plotted in Fig. 4 for all the cases discussed. A value equal to one implies closed CMTs whereas a value greater or lower corresponds to outward or inward spiraling respectively. The results show that poor accuracy in space makes the trajectories spiral outwards, especially those close to the origin, and poor accuracy in time makes them spiral inwards. From the present analysis we conclude that a 2-expansion of the number of modes in each direction of the velocity field and a second-order finite differences

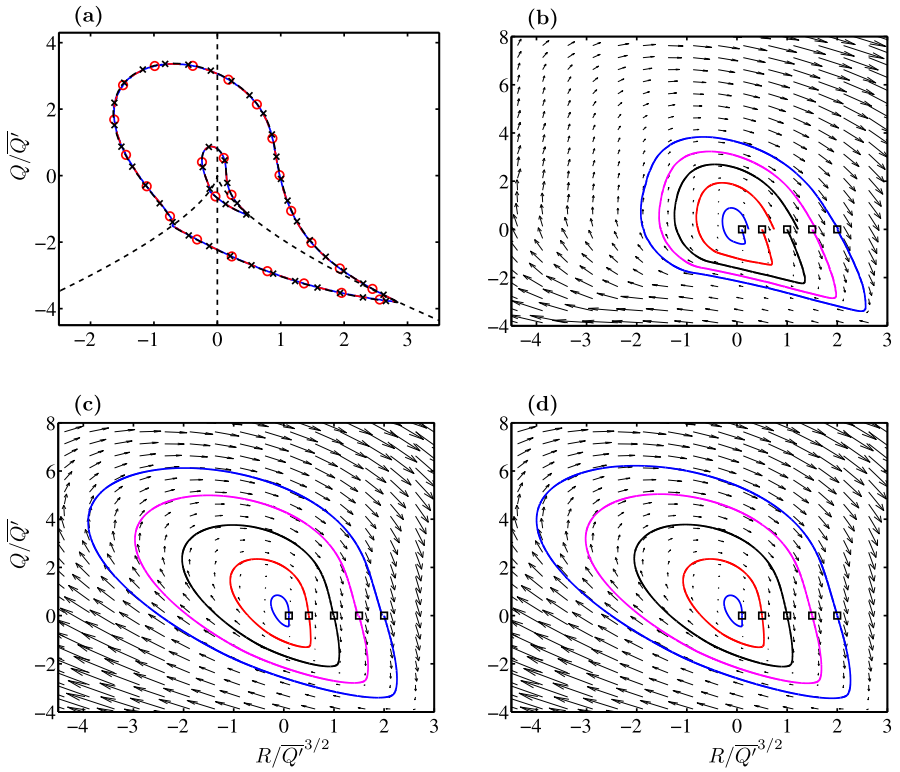

Fig. 2. (a) Joint probability density functions of the invariants of the velocity gradient, R and Q. The iso-probability contours are 50% and 98% of the data which correspond to 2.5×10^{-4} and 3.3×10^{-6} of the maximum of the p.d.f.s. Symbols and lines are ———, case E1 (3/2-expansion); ∘, case E2 (2-expansion) and ×, case E3 (3-expansion). The dashed lines are $R = 0$ and $D = 0$. Figs. (b), (c) and (d) are the conditional mean trajectories in the R–Q plane (solid lines). The trajectories are integrated from the initial conditions $(R/\overline{Q'}^{3/2}, Q/\overline{Q'}) = (0.1, 0), (0.5, 0), (1, 0), (1.5, 0)$ and $(2, 0)$ which are marked with □. The vector field is $\langle(\mathrm{D}R/\mathrm{D}t, \mathrm{D}Q/\mathrm{D}t)\rangle_{R,Q}$. (b), case E1 (3/2-expansion); (c), case E2 (2-expansion) and (d), case E3 (3-expansion).

scheme with Δt corresponding to $\mathrm{CFL} = 0.075$ is enough to produce closed CMTs with an error smaller than 1% measured as $|r_{2\pi} - r_0|/r_0$. If smaller errors are desired, a 3-expansion in space and fourth-order accuracy in time with $\mathrm{CFL} = 0.075$ yields errors below 0.1%.

4.2. Effect of a non-uniform normalization

The values of $Q'(y)$ and $R'(y)$ decay several orders of magnitude from the wall to the centre of the channel as revealed by Fig. 1(d). Then, it is reasonable to scale R and Q with a function of y which compensates for the wall-normal inhomogeneity of the channel, instead of the constant factor used in the previous sections. One natural candidate is $Q'(y)$ but it has the inconvenience of being zero at the wall and very small close to it, which turned out to be a problem. For that reason, we choose Q'_s to normalize the invariants, where $Q_s = s_{ij}s_{ij}$. Far from the wall, Q' and Q'_s follow similar trends (not shown) and it was checked that there were only minor differences above the sub-viscous layer, $y^+ < 5$, when using $Q'(y)$ or $Q'_s(y)$ to scale the invariants.

Eq. (4) is not any longer satisfied by the pair $R/Q'^{3/2}_s$ and Q/Q'_s. For example, Fig. 5(a) shows the CMTs of the non-dimensional invariants when the averaged R–Q plane velocity field is normalized as

$$\hat{\boldsymbol{v}} = \left\langle \left(\frac{\mathrm{D}R/\mathrm{D}t}{Q'^2_s}, \frac{\mathrm{D}Q/\mathrm{D}t}{Q'^{3/2}_s} \right) \right\rangle_{R/Q'^{3/2}_s, Q/Q'_s}, \tag{9}$$

and it is clear that the CMTs do not close, but rather spiral inwards. The proper quantity to compute is

$$\tilde{\boldsymbol{v}} = \left\langle \left(\frac{\mathrm{D}}{\mathrm{D}t}\left(\frac{R}{Q'^{3/2}_s}\right), \frac{\mathrm{D}}{\mathrm{D}t}\left(\frac{Q}{Q'_s}\right) \right) \right\rangle_{R/Q'^{3/2}_s, Q/Q'_s}, \tag{10}$$

and the material derivatives of Q/Q'_s and $R/Q'^{3/2}_s$ are the ones consistent with the $(R/Q'^{3/2}_s)$–(Q/Q'_s) plane in order to recover closed CMTs as shown in Fig. 5(b).

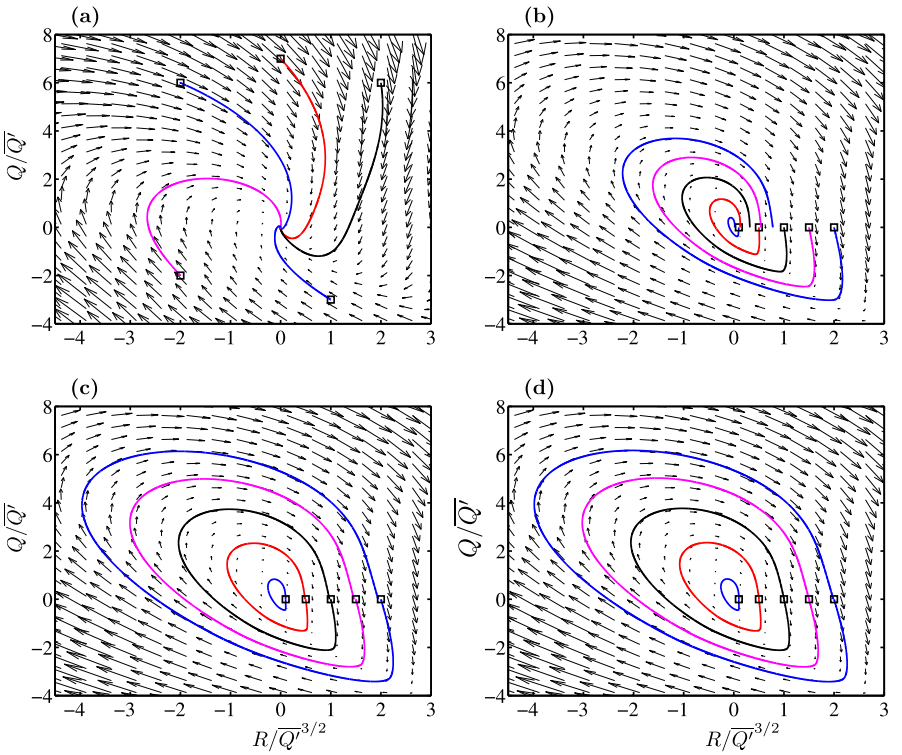

Fig. 3. Conditional mean trajectories in the R–Q plane (solid lines). The trajectories are integrated from the initial conditions $(R/\overline{Q'}^{3/2}, Q/\overline{Q'}) = (-2,6), (0,7), (2,6), (-2,-2)$ and $(1,-3)$ in (a), and $(R/\overline{Q'}^{3/2}, Q/\overline{Q'}) = (0.1,0), (0.5,0), (1,0), (1.5,0)$ and $(2,0)$ in (b), (c) and (d). The positions of the initial conditions are marked by □. The vector field is $\langle (\mathrm{D}R/\mathrm{D}t, \mathrm{D}Q/\mathrm{D}t)\rangle_{R,Q}$. (a), case F1L (1st order, CFL = 0.75); (b), case F1S (1st order, CFL = 0.075); (c), case F2L (2nd order, CFL = 0.75); (d), case F2S (2nd order, CFL = 0.075).

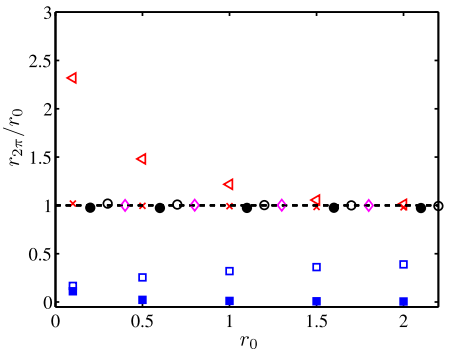

Fig. 4. Ratio of the initial distance of the CMTs to the origin of the R–Q plane, r_0, and the distance after one full revolution, $r_{2\pi}$. Symbols are ◁, case M1; ×, case M2; ◇, case M3; □, case F1L; ■, case F1S; ○, case F2L; ●, case F2S.

Note that $\widetilde{\boldsymbol{\nu}}$ is still a dimensional quantity with units of inverse of time. If $\widetilde{\boldsymbol{\nu}}$ is non-dimensionalized by $Q_s'^{1/2}$, the CMTs will not close. This can be understood considering that the contribution of all the points of the flow to $\widetilde{\boldsymbol{\nu}}$ is the same independently of their distance to the wall, i.e., they all have unit weight and their contribution is such that closed CMTs are obtained. When the material derivatives are scaled by a factor of $Q_s'^{1/2}(y)$, the points contribute differently to $\widetilde{\boldsymbol{\nu}}$ depending on their wall-normal position and this will not result in closed CMTs in general. From the physical point of view, this implies that the time cannot elapse at different rates for fluid particles at different positions from the wall if closed CMTs are desired. For that reason $\widetilde{\boldsymbol{\nu}}$ must be normalized by a constant time scale, for instance, h/u_τ.

4.3. CMTs in sub-domains of inhomogeneous flows

In the present section, we discuss the CMTs restricted to sub-domains of inhomogeneous flows such as a turbulent channel. The CMTs are computed with the same numerical accuracy as in case E3 (see Table 2).

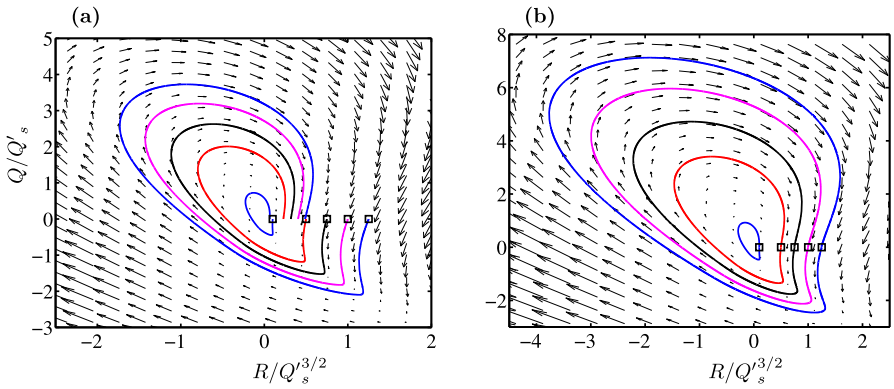

Fig. 5. Conditional mean trajectories in the $(R/Q'^{3/2}_s)$–(Q/Q'_s) plane (solid lines). The trajectories are integrated from the initial conditions $(R/Q'^{3/2}_s, Q/Q'_s) = (0.1, 0), (0.5, 0), (0.75, 0), (1, 0), (1.25, 0)$ which are marked with □. (a) CMTs integrated from the vector field in Eq. (9). (b) CMTs integrated from the vector field in Eq. (10). The invariants and their derivatives are computed with the same numerical accuracy as in case E3 from Table 2.

We divide the half bottom part of the channel in three layers: buffer, logarithmic and core region. We choose the logarithmic layer to span from $y^+ = 100$ to $y/h = 0.4$ and the buffer and core sub-domains as the regions below and above the logarithmic layer respectively. It was checked that varying those limits within the usual range [25] did not significantly alter the results presented below. The symmetry between the two walls was applied to improve the statistics by dividing the upper half of the channel in a similar manner.

The CMTs for the three regions are shown in Fig. 6 and are normalized with the constant factor $\overline{Q'}$ for Figs. 6(a, c, e) and with $Q'_s(y)$ for Figs. 6(b, d, f) following the method presented in Section 4.2 to maintain closed CMTs when the full channel is considered.

Dividing the channel in sub-domains invalidates Eq. (6). For the case with uniform normalization, the equation satisfied in a region Ω delimited by $y_1 < y < y_2$ is

$$\begin{pmatrix} \frac{\partial}{\partial R} \\ \frac{\partial}{\partial Q} \end{pmatrix} \cdot \boldsymbol{\mathcal{W}}_{\boldsymbol{\Omega}} = \phi_{\Omega}. \tag{11}$$

An analogous equation holds for the case scaled with $Q'_s(y)$. In both cases, the CMTs do not need to remain closed as confirmed by the results from Fig. 6. Indeed, the CMTs in the buffer layer spiral outward while those in the logarithmic and core regions spiral inward. The scenario is qualitatively similar for the buffer and core regions with both normalizations. However, the inward spiraling in the logarithmic region is compensated by the normalization with $Q'_s(y)$ that results in almost closed CMTs.

The results from Figs. 6(a, c, e) suggest that the outward spiraling in the buffer layer is caused by the outflow through the boundaries of fluid with large values of R and Q, and by the inflow of fluid with weak ones. The scenario is reversed in the logarithmic and core region resulting in the inward spiraling observed. A similar interpretation applies to the case with non-uniform normalization (Figs. 6(b, d, f)), with the exception of the logarithmic layer, where Q/Q'_s and $R/Q'^{3/2}_s$ change periodically without decaying (almost closed CMTs). This is probably caused by the self-similar nature of the logarithmic layer and by the balance between the incoming and outcoming normalized R and Q crossing the boundaries of the sub-domain. This behavior will be analyzed in more detail in upcoming publications.

5. Conclusions

In the present work we have studied the invariants of the velocity gradient tensor R and Q [1] in a DNS of an incompressible turbulent channel flow at $Re_\tau = 932$, and in particular their conditional mean trajectories [14].

From the theoretical analysis of the conservation of probability in the R–Q plane, we have concluded that the CMTs must be closed when the whole domain of a channel is considered, but that they spiral outward or inward if the statistics are restricted to certain subregions. This is not the case for isotropic turbulence, where the CMTs must close regardless of the sub-domain considered.

The previous statements are fulfilled when the invariants and their material derivatives are accurately computed and enough flow fields are compiled to reach statistical convergence. We have performed a spatial and temporal numerical analysis and showed that expanding the number of spatial modes of the velocity field by a factor of 3 in all the directions and computing the time derivatives with a fourth-order finite differences scheme at $\mathrm{CFL} = 0.075$ results in closed CMTs with an error smaller than 0.1% after one full revolution. Less restrictive numerical conditions may be used if higher errors are allowed. On the other hand, inaccurate computations lead to deformed CMTs and inward spiraling.

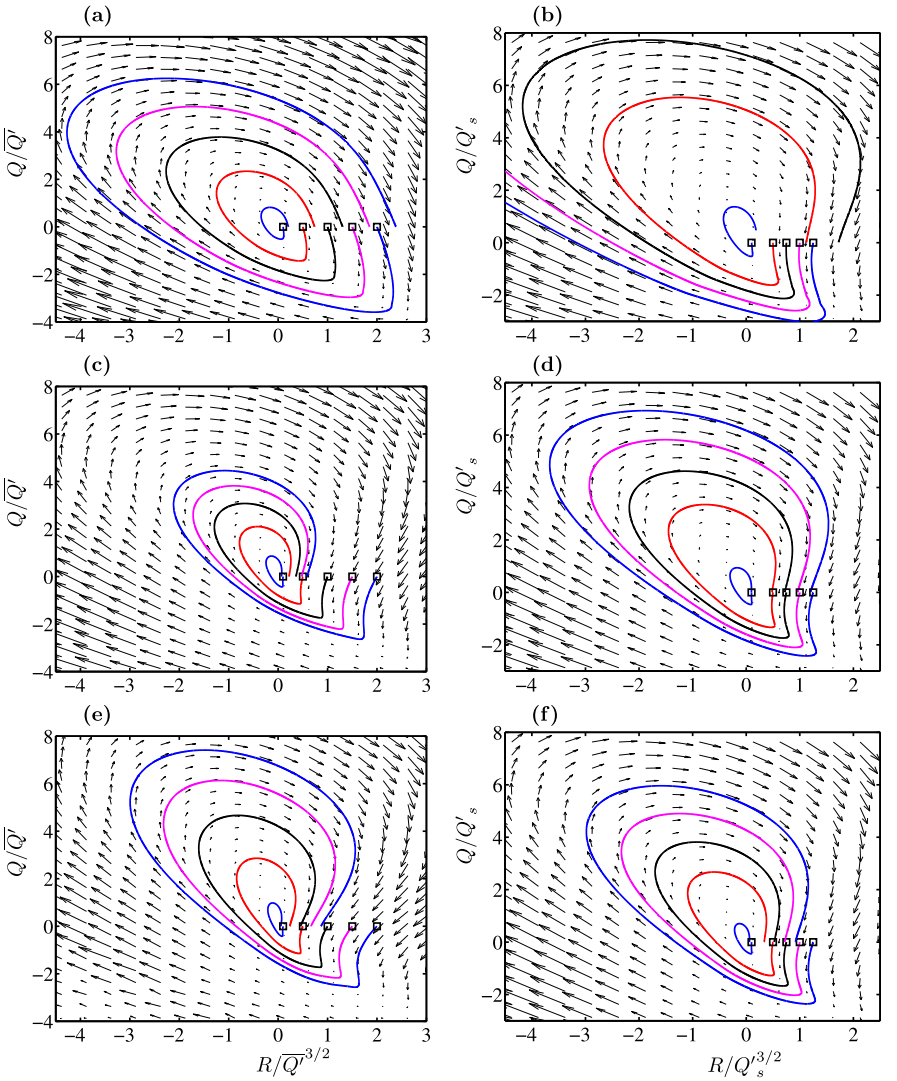

Fig. 6. (a), (c) and (e) conditional mean trajectories in the R–Q plane (solid lines) and (b), (d), (f) in the $(R/Q'^{3/2}_s)$–(Q/Q'_s) plane. The different regions are (a) and (b), buffer layer; (c) and (d), logarithmic layer; (e) and (f), core region. The trajectories are integrated from the initial conditions $(R/\overline{Q}^{3/2}, Q/\overline{Q}) = (0.1, 0), (0.5, 0), (1, 0), (1.5, 0), (2, 0)$ and $(R/Q'^{3/2}_s, Q/Q'_s) = (0.1, 0), (0.5, 0), (0.75, 0), (1, 0), (1.25, 0)$. The positions of the initial conditions are marked with □. The vector fields are $\langle (\mathrm{D}R/\mathrm{D}t, \mathrm{D}Q/\mathrm{D}t) \rangle_{R,Q}$ in (a), (c) and (e) and $\left\langle \left(\mathrm{D}(R/Q'^{3/2}_s)/\mathrm{D}t, \mathrm{D}(Q/Q'_s)/\mathrm{D}t \right) \right\rangle_{R/Q'^{3/2}_s, Q/Q'_s}$ in (b), (d) and (f). The invariants and their material derivatives are computed with the same numerical accuracy as in case E3 from Table 2.

It was also shown that using a non-uniform quantity to non-dimensionalize the invariants, in particular, when the invariants are scaled with a function that depends on the wall-normal direction, it is necessary to compute the material derivatives of the non-dimensional invariants in order to maintain closed CMTs.

Finally, the channel was divided into buffer, logarithmic and core region to study the effect of restricting the statistics of the invariants to sub-domains in an inhomogeneous flow. We have shown that in such a case the CMTs are not necessary closed and that they spiral outwards in the buffer layer, and inwards in the logarithmic and core regions. When the invariants were properly normalized using the root-mean-squared fluctuating strain as a function of the wall-normal direction, the outward and inward spirals remained in the buffer and core regions respectively, but the CMTs formed almost closed streamlines in the logarithmic region.

Acknowledgements

This work was supported in part by the European Research Council under grant ERC-2010.AdG-20100224. A. Lozano-Durán was partially supported by an FPI fellowship from the Spanish Ministry of Education and Science under project TRA2009-11498. The computations were made possible by generous grants of computer time from CeSViMa (Centro de Supercomputación y Visualización de Madrid) and from the Barcelona Supercomputing Center.

References

[1] M.S. Chong, A.E. Perry, B.J. Cantwell, A general classification of three-dimensional flow fields, Phys. Fluids 2 (5) (1990) 765–777, http://dx.doi.org/10.1063/1.857730.

[2] M. Chertkov, A. Pumir, B.I. Shraiman, Lagrangian tetrad dynamics and the phenomenology of turbulence, Phys. Fluids 11 (1999) 2394–2410.

[3] J.M. Chacin, B.J. Cantwell, Dynamics of a low Reynolds number turbulent boundary layer, J. Fluid Mech. 404 (2000) 87–115, http://dx.doi.org/10.1017/S002211209900720X.

[4] M. Tanahashi, S. Kang, T. Miyamoto, S. Shiokawa, Scaling law of fine scale eddies in turbulent channel flows up to $Re_\tau = 800$, Int. J. Heat Fluid Flow 25 (2004) 331–341.

[5] L. Chevillard, C. Meneveau, Lagrangian dynamics and statistical geometric structure of turbulence, Phys. Rev. Lett. 97 (2006) 174501, http://dx.doi.org/10.1103/PhysRevLett.97.174501.

[6] B. Lüthi, M. Holzner, A. Tsinober, Expanding the Q–R space to three dimensions, J. Fluid Mech. 641 (2009) 497–507, http://dx.doi.org/10.1017/S0022112009991947.

[7] C. Atkinson, S. Chumakov, I. Bermejo-Moreno, J. Soria, Lagrangian evolution of the invariants of the velocity gradient tensor in a turbulent boundary layer, Phys. Fluids 24 (10) (2012), http://dx.doi.org/10.1063/1.4757656.

[8] L. Wang, X.-Y. Lu, Flow topology in compressible turbulent boundary layer, J. Fluid Mech. 703 (2012) 255–278, http://dx.doi.org/10.1017/jfm.2012.212.

[9] J.I. Cardesa, D. Mistry, L. Gan, J.R. Dawson, Invariants of the reduced velocity gradient tensor in turbulent flows, J. Fluid Mech. 716 (2013) 597–615, http://dx.doi.org/10.1017/jfm.2012.558.

[10] J. Soria, R. Sondergaard, B.J. Cantwell, M.S. Chong, A.E. Perry, A study of the fine-scale motions of incompressible time-developing mixing layers, Phys. Fluids 6 (2) (1994) 871–884, http://dx.doi.org/10.1063/1.868323.

[11] A. Ooi, J. Martín, J. Soria, M.S. Chong, A study of the evolution and characteristics of the invariants of the velocity-gradient tensor in isotropic turbulence, J. Fluid Mech. 381 (1999) 141–174, http://dx.doi.org/10.1017/S0022112098003681.

[12] H.M. Blackburn, N.N. Mansour, B.J. Cantwell, Topology of fine-scale motions in turbulent channel flow, J. Fluid Mech. 310 (1996) 269–292, http://dx.doi.org/10.1017/S0022112096001802.

[13] M.S. Chong, J. Soria, A.E. Perry, J. Chacin, B.J. Cantwell, Y. Na, Turbulence structures of wall-bounded shear flows found using DNS data, J. Fluid Mech. 357 (1998) 225–247, http://dx.doi.org/10.1017/S0022112097008057.

[14] J. Martín, A. Ooi, M.S. Chong, J. Soria, Dynamics of the velocity gradient tensor invariants in isotropic turbulence, Phys. Fluids 10 (9) (1998) 2336–2346, http://dx.doi.org/10.1063/1.869752.

[15] G.E. Elsinga, I. Marusic, Evolution and lifetimes of flow topology in a turbulent boundary layer, Phys. Fluids 22 (1) (2010) 015102, http://dx.doi.org/10.1063/1.3291070.

[16] C. Meneveau, Lagrangian dynamics and models of the velocity gradient tensor in turbulent flows, Ann. Rev. Fluid Mech. 43 (1) (2011) 219–245, http://dx.doi.org/10.1146/annurev-fluid-122109-160708.

[17] P. Vieillefosse, Local interaction between vorticity and shear in a perfect incompressible fluid, J. Phys. France 43 (6) (1982) 837–842, http://dx.doi.org/10.1051/jphys:01982004306083700.

[18] P. Vieillefosse, Internal motion of a small element of fluid in an inviscid flow, Phys. Stat. Mech. Appl. 125 (1) (1984) 150–162.

[19] B.J. Cantwell, Exact solution of a restricted Euler equation for the velocity gradient tensor, Phys. Fluids 4 (4) (1992) 782–793, http://dx.doi.org/10.1063/1.858295.

[20] L. Chevillard, C. Meneveau, L. Biferale, F. Toschi, Modeling the pressure Hessian and viscous Laplacian in turbulence: comparisons with direct numerical simulation and implications on velocity gradient dynamics, Phys. Fluids 20 (10) (2008), http://dx.doi.org/10.1063/1.3005832.

[21] H. Risken, T. Frank, The Fokker–Planck Equation: Methods of Solutions and Applications, 2nd edition, Springer Series in Synergetics, Springer, 1996.

[22] A. Lozano-Durán, J. Jiménez, Effect of the computational domain on direct simulations of turbulent channels up to $Re_\tau = 4200$, Phys. Fluids 26 (1) (2014) 011702, http://dx.doi.org/10.1063/1.4862918.

[23] J. Kim, P. Moin, R.D. Moser, Turbulence statistics in fully developed channel flow at low Reynolds number, J. Fluid Mech. 177 (1987) 133–166.

[24] R.D. Moser, J. Kim, N.N. Mansour, Direct numerical simulation of turbulent channel flow up to $Re_\tau = 590$, Phys. Fluids 11 (4) (1999) 943–945, http://dx.doi.org/10.1063/1.869966.

[25] I. Marusic, J.P. Monty, M. Hultmark, A.J. Smits, On the logarithmic region in wall turbulence, J. Fluid Mech. 716 (2013) R3, http://dx.doi.org/10.1017/jfm.2012.511.